energy&fuels

pubs.acs.org/EF

Article

Chemical Route Synthesis of Nanohybrid Mo−V Oxide and rGO for High-Performance Hybrid Supercapacitors

Ganesh V. Dilwale, Anuradha C. Pawar, Guanghai Piao, Qian Wang, Zafar Said, Rajesh K. Nimat,* Jung Bin In,* Ji Man Kim,* and Ravindra N. Bulakhe*

Cite This: *Energy Fuels* 2024, 38, 13355−13364

Read Online

ACCESS | Metrics & More | Article Recommendations | Supporting Information

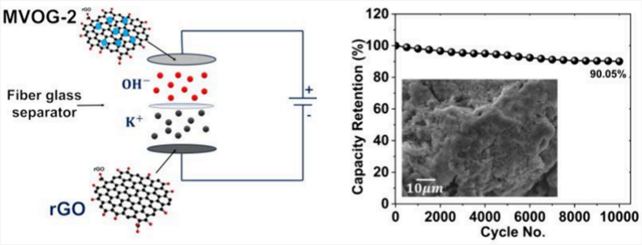

ABSTRACT: High-performance hybrid supercapacitors (HSCs) have been developed by combining two different electrode materials with wide potentials and long cycling stabilities. To develop high-performance HSCs, molybdenum vanadium oxide (MVO) was hybridized with graphene oxide (GO). The system of hydrothermal chemical pathways was used to synthesize the MVO/rGO (MVOG) nanohybrid material. The optimal MVOG achieves the highest specific capacity of 714.85 C/g compared to the bare MVO of 270.73 C/g at a sweep rate of 2 mV/s. The HSC was fabricated with two electrodes, namely, optimal MVOG and rGO as cathode and anode, respectively. The HSCs exhibit a maximum capacity of 185.06 C/g, with an operating potential of 1.5 V in 2 M KOH, with a maximum energy and power density of 38.55 Wh/kg and 2434.38 W/kg, respectively. The investigation conducted in this study reveals that the hybridization of MVO with GO enhances the physiochemical and electrochemical properties. The prepared MVOG electrode shows a 3-fold increase in supercapacitive efficiency compared to the MVO electrode. Different nanohybrids using ternary metal oxides with rGO can be developed by the same chemical route and hybridization method.

1. INTRODUCTION

Hybrid supercapacitors (HSCs) represent a promising class of energy storage devices that amalgamate the advantages of both conventional supercapacitors and batteries. These devices have garnered significant attention in recent years owing to their potential to address the limitations of existing energy storage technologies.[1] The development of high-performance HSC has been the focus of research, because of the increasing demand for efficient energy storage systems. A promising approach to enhance the electrochemical performance of these devices is the development of nanohybrid materials by combining transition metal oxides with reduced graphene oxide (rGO).[2] Recent developments in the field of energy storage devices, electronic-based communications, memory devices, electric vehicles, and the use of high power in a very short time are all related to electrochemical purposes.[3] HSC have recently received attention because of the demand for integrated energy storage and conversion systems.[4,5] Hybrid supercapacitors offer high power density similar to conventional supercapacitors, along with improved energy density comparable to batteries, making them ideal candidates for various applications ranging from portable electronics to electric vehicles and grid-level energy storage systems.[6]

Recent progress in hybrid supercapacitor research and development has led to significant advancements in materials science, device architecture, and performance optimization. Novel electrode materials, electrolyte formulations, and fabrication techniques have emerged that enable enhanced energy storage capabilities, improved cycle life, and superior electrochemical performance. Moreover, advancements in nanotechnology and additive manufacturing have facilitated the precise engineering of hybrid supercapacitor components at the nanoscale, further enhancing their efficiency and scalability.[7]

Despite the remarkable progress achieved in the field, several challenges remain to be addressed to fully unlock the potential of hybrid supercapacitors. Key challenges include the development of cost-effective and environmentally sustainable materials, optimization of electrode−electrolyte interfaces to minimize internal resistance and maximize energy storage capacity, and improvement of device stability and durability over prolonged cycling. Additionally, the scalability of manufacturing processes and the integration of hybrid supercapacitors into existing energy storage infrastructures present logistical and technological challenges that require innovative solutions.[8]

Received: January 7, 2024
Revised: June 17, 2024
Accepted: June 18, 2024
Published: July 3, 2024

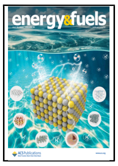

ACS Publications

https://doi.org/10.1021/acs.energyfuels.4c00094

To improve the energy density and long life, several binary metal oxides have been studied. For example, $MnCo_2O_4$ has a specific capacity of 126 C/g at 1A/g,[9] $NiFe_2O_4$ using urea as a precipitant shows the maximum capacity of 337.26 C/g at 1 A/g,[10] and the hierarchical mesoporous structure of $NiCo_2O_4$ possesses an outstanding 1006 C/g capacity at 1 A/g. Even at 10 A/g, the material exhibits a 451.5 C/g specific capacity.[11] The mesoporous Co−Ni−Zn ternary oxide nanosheet shows a mesoporous structure (75.4 m^2/g), with specific capacity of 1172.2 C/g at 1 A/g, and high-capacity retention of 78.8% over 2500 cycles, respectively.[12] These materials exhibit excellent electronic conductivity, enhanced structural stability, and ability to tune redox potentials.[13] Still, binary metal oxides have certain limitations, poor conductivity, and low surface area when used alone. The integration of binary metal oxides with other materials, such as nitrogen-doped graphene and conducting polymers, further enhances their properties. Hence, to enhance the performance of SCs, many molybdenum- and vanadium-based binary metal oxides have been studied.[14] Electrochemical performance of α-$MnMoO_4$ with different electrolytes was studied, and the maximum specific capacitance was 1297.4 C/g at 5 mV/s in H_2SO_4 electrolyte.[15] The catalyst-free growth of single-crystalline β-$Na_{0.33}V_2O_4$ nanowire shows a specific capacity of 415 C/g at 0.4 A/g.[16] Until today, SC application reports based on molybdenum vanadium oxides are rare.

HSCs are fabricated using a combination of a porous carbon electrode and metal oxides, conducting polymers, or metal-doped carbons. This electrode setup, which combines a high-pseudocapacitance electrode with a high-double-layer-capacitance electrode, produces high specific powers and energy densities.[17] The electrochemical performance mainly depends on the structural and electronic properties of the material.[18] Due to their maximum capacity, energy, and power density, as well as excellent cycling stability, HSCs are the most attractive devices. Nanocomposite-based HSCs provide higher specific capacities than electric double-layer capacitors (EDLC) and pseudocapacitors due to the two types of electrode materials containing different charge storage characteristics.[19] Currently, researchers are successfully developing HSC devices with a wide operating potential range, good cycling stability, and improved electrochemical behavior. Furthermore, nanocomposite materials can increase the surface area, providing numerous electrochemically active sites. rGO has superior electrical properties; hence, it has been used in SC, lithium-ion batteries, and stretchable electronics.[20]

So far, various nanohybrid materials based on metal oxide and rGO have been used, including an rGO//$BiVO_4$ fern-like hybrid nanostructure with a specific capacitance 241.6 C/g at 0.15 mA/cm^2.[21] The α-$MnCo_2O_4$@$NiMoO_4$//Activated carbon device produces 42 Wh/kg energy density and 852.3 W/kg power density with 93% capacity retention over 8000 cycles.[22] Similarly, the asymmetric supercapacitor device α-Fe_2O_3/NiO/rGO produces 35.38 Wh/kg energy density at 558.6 W/kg and retains 94.52% capacity over 5000 cycles at 1 A/g[23] and the synergistic impact of Ppy additive in rGO/$MnFe_2O_4$/Ppy shows a specific capacity of 232 C/g.[24] Also, the asymmetric α-Fe_2O_3/MnO_2/rGO device delivers an energy density of 13.2 Wh/kg at a power density of 6124 W/kg with 92% capacitance retention over 5000 cycles at 10 A/g and a specific capacity of 135.8 C/g at 1 A/g.[25] The aforementioned results indicate that hybrid materials can be used as efficient electrodes in HSC applications to create reliable, high-rate capability, high specific capacity, good power density, durable life, and efficient energy storage devices.

Vanadium oxide (VO) exhibits a high specific capacity of 1474 mAh/g for Li^+ intercalation, but it suffers from low conductivity and stability during cycling.[26] Also, the molybdenum oxides (MoO_2 and MoO_3) show high theoretical specific capacities of about 838 mAh/g for dioxide and 1117 mAh/g for trioxides.[27] Molybdenum is a well-known multivalent element, with oxidation states ranging from −2 to +6. It exhibits a similar redox potential to vanadium and compatible crystallographic characteristics, such as compatible ionic radii and coordination.[28] Thus, ternary material based on molybdenum−vanadium oxide (MVO) provides redox couples, and it can help in intercalation/deintercalation processes and also reduce the charge/ion transfer path length during the process, which can lead to improvement in electrochemical performance.[29] Thus, the motive behind the choice of MVO is to achieve very high specific capacity. By synthesizing nanohybrid materials, MVO-rGO (MVOG) can overall improve the electrochemical performance as per the research studied so far.

This paper aims to explore and demonstrate a single step hydrothermal synthesis method for synthesizing nanohybrid materials such as the Mo−V oxide and rGO. The primary focus of this synthesis approach is to synthesize materials with enhanced electrochemical properties suitable for high-performance hybrid supercapacitors. This article intends to investigate the structural, morphological, and electrochemical characteristics of the synthesized nanohybrid material. This investigation includes detailed analyses of the structure and composition of the hybrid material. Additionally, the electrochemical performance of the resulting hybrid material, including its specific capacitance, cycling stability, and rate capability, was thoroughly evaluated.

Overall, the research paper seeks to contribute to the advancement of supercapacitor technology by presenting a viable synthesis route for nanohybrid materials that offer improved energy storage capabilities. These materials hold promise for various energy storage applications. In this study, a simple, single-step hydrothermal chemical route method was utilized to synthesize MVO and MVOG nanohybrids. The advantage of this synthesis method lies in the simultaneous reduction of GO to rGO and the synthesis of MVO, with the growth and size of nanoparticles easily controllable by varying the deposition parameters. The effects of different amounts of GO solutions (5, 10, and 15 wt %) in bare MVO were successfully hybridized, and the prepared MVOG nanohybrid electrodes were further studied for physicochemical and electrochemical performance. Hybrid MVOG and rGO nanosheets were employed as positive and negative electrodes in the fabrication of the HSC device. To the best of our knowledge, the MVOG nanohybrid material has been tested for supercapacitor application for the first time.

2. MATERIALS AND METHODS

2.1. Materials. Analytical reagents ammonium metavanadate [NH_4VO_3] ACS reagent ≥99.0%, ammonium heptamolybdate [$(NH_4)_6Mo_7O_{24}\cdot 4H_2O$] ACS reagent ≥99.5%, tartaric acid [$C_4H_6O_6$], and nitric acid [HNO_3] were purchased from S D Fine Chem Limited (SFCL). Highly dispersed graphene oxide, potassium hydroxide (KOH) purity ≥99.99%, polyvinylidene difluoride [PVDF] $(CH_2CF_2)_n$ with a purity >99.90%, Ni foam with a purity >99.90% (3 × 10 × 50 mm^3), and doubled distilled water purity >99.9% were purchased from Sigma Aldrich and used to prepare the electrode without further purification. The details of chemicals are discussed in note S1 of the Supporting Information.

2.2. Methods (Preparation of MVOG Nanohybrids). The glassware was cleaned with care. Tartaric acid [$C_4H_6O_6$] is added to 80 mL of distilled water to dissolve 0.01 M ammonium metavanadate [NH_4VO_3]. The mixture was stirred until all of the solute's particles were dissolved in the water. After that, a few drops of nitric acid [HNO_3] and 0.01 M ammonium heptamolybdate [$(NH_4)_6Mo_7O_{24}\cdot 4H_2O$] were added to the solution until becomes PH 3. The resulting mixture was continually stirred until it was a clear yellow color. The resulting mixture was then put in a 120 mL Teflon bottle and tightly sealed in the autoclave. After that, the autoclave was placed in a heating reactor for a 12 h reaction period with a 180 °C temperature maintained. The dark blue/black colored solution was filtered out after cooling, and a dark blue/black colored powder was collected. The collected powder was then subjected to a 4 h annealing process at 400 °C for further characterization needs. In order to prepare the MVOG nanohybrid materials, GO solution (5 mg/mL) was added to the above obtained solution under the same experimental conditions. The detailed chemical reaction for synthesis of MVO is described in Supporting Information note S2.

2.3. Material Characterization and Electrochemical Analysis. Various characterization techniques were used to study the physiochemical and electrochemical properties of the MVO and MVOG nanohybrids. Importantly, an X-ray powder diffractometer (Cu Kα λ = 1.54 Å) was used to investigate the crystalline phase and structural properties of the prepared nanohybrid materials. Scanning electron microscopy (SEM) was used to analyze the surface of the nanohybrid materials. Energy dispersive spectroscopy (EDS) was employed for elemental composition analysis and mapping. High-resolution transmission electron spectroscopy (HR-TEM) was used to detect the atomic structure of the samples with high resolution. The X-ray photoelectron spectroscopy (XPS) technique was utilized to study the surface chemistry and chemical states. The BET technique was used to analyze the surface and porosity of the material. A Bio-Logic 150 potentiostat was used to analyze the electrochemical properties of samples in 2- and 3-electrode systems. The details about the Characterization techniques are discussed in note S4 of the Supporting Information.

3. RESULT AND DISCUSSION

3.1. Physiochemical Properties of MVO and MVOG.

By preparing several nanohybrids using varied proportions of GO (5, 10, and 15 mL), the hybridization capacity of MVO was examined. The resulting MVOG nanohybrids were designated MVOG-1, MVOG-2, and MVOG-3, respectively. Figure 1(a) shows the X-ray diffraction (XRD) analysis of bare MVO and MVOG nanohybrids. The most intense peak is observed at angle 2θ = 21.270°, which belongs to the (001) plane. The X'pert high score plus software was used to identify and match the peaks. Additionally, we get the information regarding phase and crystallinity of MVO and MVOG nanohybrid materials.

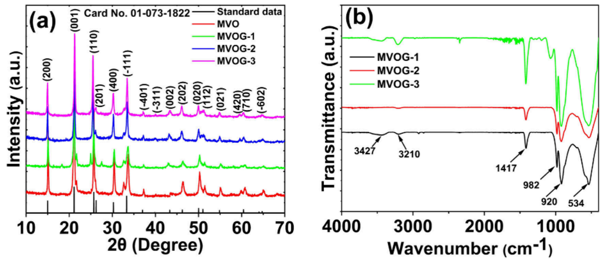

Figure 1. (a) XRD spectra and (b) FTIR of MVO and MVOG nanohybrids materials.

The empirical formula/chemical formula of the compound formed is $Mo_{0.56}V_{1.44}O_5$ (molybdenum vanadium oxide) and shows nonstoichiometry. The XRD pattern of MVO and MVOG nanocomposites shows the same stoichiometry with ICSD card number 01-073-1822 and the space group C2(5) indicates that the crystal surface is predominant in the monoclinic crystal structure for all MVO and MVOG-1, -2, and -3 nanohybrids. The majority of high-intensity peaks were matched with the standard data. Also, some minor intensity peaks were observed, and this may correspond to incoherent scattering of incident X-rays with the impurities atoms present in the sample.[30]

The d spacing values are calculated from X-ray diffraction pattern using the Bragg's equation

$$d = \frac{n\lambda}{2\sin\theta} \quad (1)$$

The interplanar spacings for each plane were calculated and are represented in Table S1. Particularly for the planes (110) and (400), the d values are 0.3463 and 0.2934 nm, respectively. This d value exactly matches with interplanar spacing using HRTEM.

The role of rGO in the MVOG composite is to enhance the conductivity and, thereby, enhance the energy density of the hybrid material by increasing the number of active sites in the MVO material. This clearly indicated that rGO did not alter the MVO crystal structure.[31] The existence of each of these diffraction peaks demonstrates the polycrystalline nature of the prepared MVO and MVOG nanohybrids. The rGO peaks are absent in the XRD patterns; hence, XPS spectroscopy was investigated to confirm the hybridized MVO with rGO.

Figure 1(b) shows the FTIR spectra of all MVOG nanohybrid materials and confirms the formation of nanohybrid materials with the presence of the functional groups in the samples. The band at 534 cm^{-1} has been assigned to the symmetric vibrational bonds for V−O−V.[32] The presence of absorption peak at 920 cm^{-1} indicates the presence of V^{4+}.[33] The absorption peak at 981 cm^{-1} is assigned to the Mo-terminal oxygen linked with two or three Mo atoms (asymmetric stretching of Mo_2−O)[34] and the peak at 1417 cm^{-1} is assigned to C−C functional moieties of the graphene nanosheet. The small absorption bands at 3427 and 3210 cm^{-1} are attributed to the O−H stretching and to the N−H symmetric stretching, respectively.[35]

3.2. XPS Analysis. The elaborated details regarding elemental composition and various oxidation states of MVO and MVOG electrodes are characterized by XPS study and Figure S1(a), the complete survey spectrum of MVO and MVOG nanohybrids shows the presence of Mo, V, O, and C elements in the samples. Figure 2(a) represents the Mo 3d X-ray emission spectrum in MVOG-2, and Figures S1(b), S2(a), and S3(a) represent Mo 3d XPS fitting for MVO, MVOG-1, and MVOG-3 samples, respectively. It comprises two spin−orbit doublet peaks. The high-resolution X-ray emission spectra are fitted using the Voigt function with the help of Origin software. The fitted XPS peaks of Mo 3d in MVOG-2 with binding energies of 229.8, 231.16, and 232.64 eV are assigned to Mo^{4+} $3d_{5/2}$, Mo^{5+} $3d_{5/2}$, and Mo^{5+} $3d_{5/2}$. Also, the binding energies 233, 234.5, and 236.1 eV are attributed to Mo^{4+} $3d_{3/2}$, Mo^{5+} $3d_{3/2}$, and Mo^{5+} $3d_{3/2}$.[36] The binding energy difference between corresponding Mo $3d_{3/2}$ and Mo $3d_{5/2}$ is in the range 3.1−3.5 eV and details are shown in Table S2. As a result of multiple oxidation states existing in Mo 3d, it can

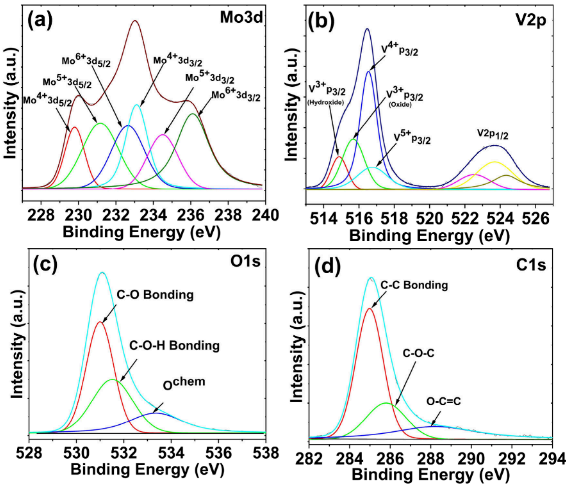

Figure 2. High-resolution XPS spectra of MVOG-2 nanohybrid, (a) Mo 3d, (b) V 2p, (c) O 1s, and (d) C 1s.

transfer multiple electrons to enhance Faradaic redox processes and prolong discharge time. The most stable oxidation state of Mo is the Mo^{4+} 3d state. The full width at half-maximum (FWHM) value of the Mo^{4+} 3d state decreases in the case of MVOG-2 as compared with that of MVO and thereby increases in % relative peak intensity. It is observed that there is a slight shift in the position of Mo 3d oxidation peaks in MVOG, and this shift may be due to hybridization of MVO with rGO. Also, the binding energies corresponding to different oxidation states, FWHM of individual oxidation peaks, and % relative peak intensity are shown in Table S3. In addition, due to hybridization of MVO with rGO, the % relative peak intensity in MVOG is higher as compare with that of MVO.[37]

Figure 2(b) shows the high-resolution X-ray spectrum of the V 2p state in the MVOG-2 sample. Also, the XPS spectrum of V 2p of MVO, MVOG-1, and MVOG-3 is shown in Figures S1(c), S2(b), and S3(b), respectively. The fitted XPS peaks of V 2p in the MVOG-2 sample have binding energies 514.87, 151.67, 516.53, 516.75, 522.52, and 524.33 eV assigned to V^{3+} $2p_{3/2}$ (hydroxide), V^{3+} $2p_{3/2}$ (oxide), V^{4+} $2p_{3/2}$, $V^{5+}2$ $p_{3/2}$, V $2p_{1/2}$ (I), and V $2p_{1/2}$ (II).[38] Vanadium also consists of four different oxidation states. The most stable state of V 2p is V^{4+} $2p_{3/2}$ with a B.E. 516 eV.[39] The binding energies corresponding to different oxidation states, FWHM of individual oxidation peaks, and % relative peak intensity are shown in Table S4. It is observed that the peak intensity of the most stable V 2p state in MVOG-2 is increased as compared with those of MVO, MVOG-1, and MVOG-3 due to hybridization. Also, the FWHM value decreases, thereby increasing the % relative peak intensity. Figure 2(c) shows the XPS spectrum of O 1s of the MVOG-2 nanohybrid material. The B.E. values 531, 531.5, and 533.3 eV correspond to C−O, C−O═H, and bonding due to the chemical environment in the MVOG-2 sample.[40] In addition, the XPS spectra of O 1s of MVO, MVOG-1, and MVOG-3 are shown in Figures S1(d), S2(c), and S3(c), respectively. The FWHM values and % relative intensity of MVO and MVOG-2 for O 1s are shown in Table S5. Figure 2(d) represents the fitted XPS spectrum of C 1s in the MVOG-2 sample. The B.E. values 284.99, 285.79, and 288.21 eV are attributed to C−C, C−O−C, and O−C═C.[41] Also, the XPS spectra of C 1s of MVOG-1 and MVOG-3 are shown in Figures S2(d) and S3(d), respectively. It was found that the peak intensity of the optimized MVOG-2 nanohybrid was higher than that of the MVO and MVOG-1 and MVOG-3 nanohybrids. This was caused by the fact that there were more atoms in each of the oxidation states and that more of them diffused toward the surface, increasing the peak intensity.[42] The quantitative analysis of MVO, MVOG-1, MVOG-2, and MVOG-3 is represented in Tables S6−S9. Also, the carbon to oxygen ratio is calculated from atomic % using XPS, and it is observed that for MVOG-2, the C/O ratio is 1.098, which is the maximum as compared to those of MOG-1 and MOG-3, as mentioned in Table S10.

3.3. Morphological Analysis. The morphological study of the MVO and MVOG nanohybrid materials was investigated to determine the crystal sizes and shapes analyzed by scanning electron microscopy (SEM). Figure 3(a) represents the SEM MVO image, which shows a flower-like morphology at a resolution of 5 μm. These flowers are formed by connecting the nanostrips during hydrothermal synthesis. Similarly, the nanohybrid MVOG-2 shows the morphology of the dispersed nanostrips (like dispersed flower petals) wrapped with the layered rGO nanosheet with a resolution of 5 μm depicted in Figure 3(b). The elemental composition, distribution, and EDS spectrum in the nanohybrid MVOG-2 were investigated by EDS and are shown in Figure S4. All elements (Mo, V, O, and C) are uniformly distributed over the entire scanned area, indicating homogeneous hybridization of MVO and rGO. Elemental compositions of MVO using EDAX are depicted in Table S11.

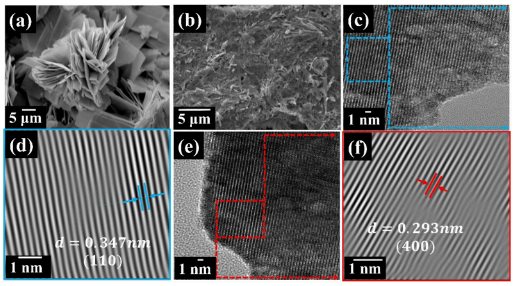

Figure 3. SEM images of (a) MVO and (b) MVOG-2, at 5 μm resolution. HR-TEM images of (c) MVO and (d) *d*-spacing for MVO sample and of (e) MVOG-2 and (f) *d*-spacing for MVOG-2 sample at 1 nm resolution.

Figure 3(c,e) shows the HR-TEM image of the MVO and MVOG-2 nanohybrid at a resolution of 1 nm. This technique is used to examine the growth crystal structures and shapes.[43] Figure 3(d) also shows the TEM images of MVOG at a high resolution of 1 nm, which clearly shows the atomic planes with a *d* spacing of 0.347 nm, which corresponds to the (110) plane as compared with XRD data. The magnified image of the TEM image with *d* spacing is calculated using Gatan software. Figure 3(e) shows the aligned lattice fringes with the observed lattice spacing value *d* equal to 0.293 nm, which corresponds to the (400) lattice plane, confirmed by the XRD diffraction pattern. Similarly, Figure S5(a,b) shows the HRTEM image of MVO and MVOG-2 at 0.5 μm resolution. Figure S5(c,d) shows the HRTEM image of MVO and MVOG-2 at 100 nm resolution. Figure S5(e,f) represents the selected area diffraction pattern (SAED) with *hkl* planes indexed for the MVO and MVOG-2 nanohybrid at resolution 10 $(nm)^{-1}$. The live profile of the interplanar *d* spacing of MVOG-2 is shown in Figure S6(a,b).

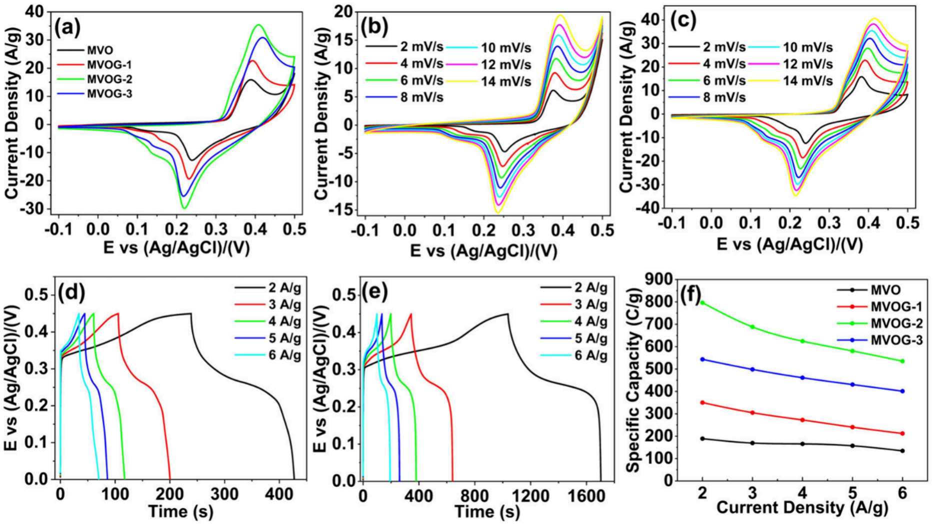

Figure 4. Cyclic voltammograms of (a) MVO and MVOG-2 nanohybrids at a sweep rate of 10 mV/s, (b) MVO and (c) MVOG-2 electrodes at sweep rates (2−14 mV/s), and galvanostatic charge−discharge graphs of (d) MVO and (e) MVOG-2 at current densities ranging from 2 to 6 A/g. (f) Specific capacities of MVO and MVOG nanohybrids at various current densities.

The quantitative SAED analysis of MVOG-2 nanohybrid is done with the help of ImageJ software, and the detail calculation is provided in Table S12. Figures S7 and S8 represents the EDS elemental line mapping of the MVOG-2 nanohybrid using HR-TEM. The quantitative analysis of MVOG-2 using HRTEM line mapping table is shown in Table S13.

3.4. Electrochemical Measurements. The electrochemical analysis of the bare MVO and MVOG nanohybrid composite was performed using a three-electrode system. MVO/MVOG is used as the working electrode, Pt chip as the counter electrode, and *E* vs (Ag/AgCl)/V as the reference electrode, respectively. The detailed preparation of the reduced graphene oxide (rGO) electrode is described in Supporting Information note S3. Combined cyclic voltammetry (CV) graphs of the MVO and MVOG nanohybrids at a sweep rate of 10 mV/s in the 2 M KOH electrolyte are shown in Figure 4(a). The optimal MVOG-2 electrode shows high capacity compared to other electrodes, which is confirmed by the larger area under the graphs. Figure 4(b,c) represents CV graphs for bare MVO and MVOG-2 at sweep rates from 2 to 14 mV/s with a potential of 0.6 V having a range from −0.1 to +0.5 V. Thus, the hybridization of MVO with rGO raises the current density as compared to bare MVO. This increase in current density results from the increase in the number of conducting channels, low internal resistance, increase in the porosity of the composite material, and the flow of ions between the electrodes and the electrolyte.[44]

All MVO and MVOG nanohybrid electrodes exhibit specific redox pairs associated with Faradaic reversible redox responses ranging from MoV_2O_5 to $MoV_2O_{5-x}OH_x$. The prominent redox pair, occurring between approximately 0.195 and 0.336 Ag/AgCl (V), corresponds to reversible redox reactions involving Mo^{5+} to Mo^{4+} transformations. Conversely, the predominant redox pair within the potential range 0.238−0.3830 V in MoV_2O_5 is attributed to the redox reaction linked to Mo^{6+} to Mo^{5+} transformation, as shown in Figure S18. These redox pairs signify the intercalation of OH^- ions into the MVO matrix during charging, while deintercalation of electrolyte ions occurs during discharging, as illustrated in the following reaction[45]

$$MoV_2O_5 + xOH^- \leftrightarrow MoV_2O_{5-x}OH_x + xe^- \quad (2)$$

Also, the CV analysis at sweep rates from 2 to 14 mV/s with a potential of 0.6 V having a range −0.1 to +0.5 V for the MVOG-1 and MVOG-2 nanohybrid electrodes is shown in Figure S9(a,b) respectively. The CV graphs for these electrode materials exhibit redox peaks, and the shapes are not rectangular, indicating pseudocapacitive charge storage mechanisms. As a result of hybridization, an increase in the area under the CV graphs is observed (increase in the current and broadening of redox peaks). The difference between the positive and negative potential ($\Delta E_{c,a}$) is 150.8, 159.2, 188.4, and 203.5 mV corresponding to MVO, MVOG-1, MVOG-2, and MVOG-3. Thus, MVOG-2 ($\Delta E_{c,a}$) is smaller compared to the rest of the electrodes, indicating that it shows high reversibility in electrochemical redox reactions. The current response and ($\Delta E_{c,a}$) of these electrodes increase with the sweep rates.[46] The cathodic and anodic peaks shifted toward positive and negative potentials due to the combined effect of capacitive-controlled and diffusion-controlled currents.

At higher scan rates, the charge storage behavior is mainly dominated by the surface-controlled, i.e., capacitive-controlled, process, while at low scan rate, the diffusion-controlled process predominates.[47] As per power law, understanding the electrochemical kinetics using the cyclic voltammetry is provided by[48]

$$i = av^b \quad (3)$$

where i is the peak current value, a and b are tunable constants, and v is the scan rate. Typically, a b value of 0.5 signifies a diffusion-controlled process, while a b value of 1 indicates a capacitive-controlled process. Figure 5(a) represents the CV of MVO at scan rates 2−14 mV/s and corresponding peak anodic and cathodic current values.

The b value is calculated from the graph of log i versus log v, as shown in Figure 5(b). The list of the diffusion coefficients in oxidation and reduction, along with the b values for MVO and MVOG materials, are tabulated in Table S15. The obtained b value of MVO is 0.59, which indicates both capacitive-

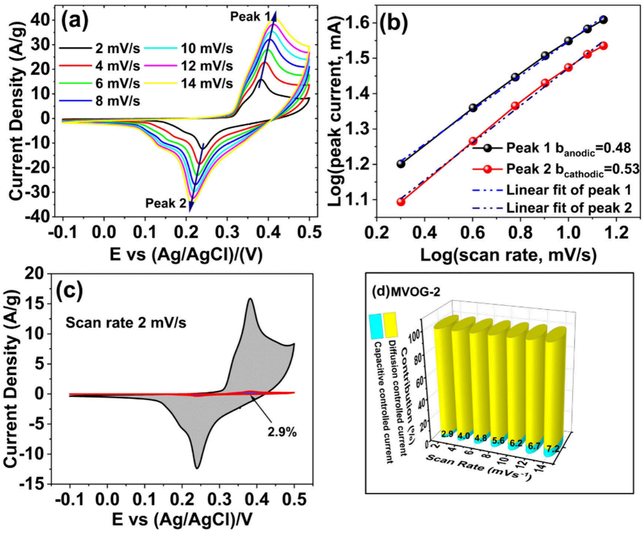

Figure 5. Electrochemical kinetics measurement of MVOG-2 electrode: (a) CV curves performed at 2−14 mV/s scan rates and (b) the corresponding linear fitting from (a) cyclic voltammograms based on log *i* against log *v* plots. (c) Capacitive contribution depicted in blue shadow (red boarder) area at 2 mV/s and (d) proportion contribution of capacitive and diffusion-dominant capacities at diverse scan rates.

controlled and diffusion-controlled processes are active but slightly dominate the capacitive-controlled process due to the pseudocapacitive nature of the MVO material. While *b* values for MVOG decreases with increase of GO concentration, which suggests that the process is shifting toward diffusion-controlled.[49] The detailed quantitative analysis of diffusion and capacitive contribution is analyzed by Dunn method using following equation

$$i = k_1 v + k_2 v^{1/2} \tag{4}$$

where k_1 and k_2 are parameters, $k_1 v$ corresponds to the capacitive-controlled current, and $k_2 v^{1/2}$ corresponds to the diffusion-controlled current.

At higher scan rates the rapid electron/ion transport and intercalation/deintercalation processes favor capacitive behavior, where charge accumulation and release occur more readily on the electrode surface and vice versa with diffusion-controlled processes. It involves slower mass transport within the electrode materials and becomes relatively less significant at elevated scan rates. Consequently, capacitive components predominate over diffusion-controlled components in the MVO and MVOG materials. Figure 5(c) shows the capacitive contribution CV area at 2 mV/s, which is about 2.9% of the total area. Also, Figure 5(d) shows the proportional contribution of capacitive and diffusion-dominant capacities at diverse scan rates. Tables S16 and S17 shows that with increase in scan rates capacitive-controlled process is dominating to diffusion-controlled process for anodic as cathodic peaks. Figure S10(a) shows the variation of cathodic and anodic peak current with square root of scan rate and Figure S10(b) corresponding linear fitting of MVO, MVOG-1, MVOG-2, and MVOG-3, respectively. Similarly, the contribution of diffusion-controlled current and capacitive-controlled current for MVO, MVOG-1, and MVOG-3 are shown in Figures S11, S12, and S13, respectively.

The optimized MVOG-2 nanohybrid electrode shows a capacity of 714.8 C/g at a sweep rate of 2 mV/s due to the presence of 3 wt % GO in the MVOG-2 nanohybrid. The increase in MVOG conductivity results from the uniform distribution of MVO with rGO.[50,51] The specific capacity calculations are carried out with the help of equations as shown in Supporting Information note S6.

The investigation of the electrochemical performance of the MVO and MVOG nanohybrid electrodes were carried out by galvanostatic charge−discharge (GCD) and electrochemical impedance spectroscopy (EIS). Figure 4(d,e) and Figure S9(c,d) illustrate the GCD graphs of MVO and MVOG-2, MVOG-1, and MVOG-3 at (2−6 A/g), respectively. The MVO, MVOG-1, and optimized MVOG-2 and MVOG-3 capacity values were 188.86, 350.19, 796.25, and 543.13 C/g at 2 A/g, respectively. The MVOG nanohybrid electrode shows better electrochemical performance than MVO due to the incorporation of reduced graphene oxide into the host material.[52] A similar study of the Mo-doped V_2O_5 material was carried out for the lithium-ion battery,[53,54] due to the battery-type nature of MVO materials. On the other hand, rGO has high electrical conductivity, which provides high charge mobility to the attached MVO particles.[55]

rGO acts as an EDLC electrode material, synergistically enhancing the performance of the MVOG composite. However, increasing the mass loading of rGO leads to a reduction in the contribution of MVO particles to the overall capacity. This phenomenon is commonly observed in various graphene-based supercapacitors, where excessive rGO impedes ion and charge mobility, thereby diminishing charge storage capacity.[56] Consequently, MVOG-2 demonstrates superior electrochemical performance compared to those of MVOG-1 and MVOG-3. In the case of MVOG-3, where the GO solution volume was increased to 15 mL, a decline in electrochemical performance was observed relative to MVOG-2. This reduction is likely due to the excessive GO masking of the active sites of the MVO component, hindering its effectiveness. This highlights the importance of optimizing the balance between the rGO and MVO components to maximize the electrochemical performance of the composite.

Electrochemical results of the present 3-electrode system and various previously reported energy storage materials are shown in Table S14. Figure 4(f) shows the response of the specific capacity (C/g) with the current density (A/g) of the MVO and MVOG nanohybrid electrodes. Figure S9(e) shows the capacity retention of bare MVO, MVOG-1, MVOG-2, and MVOG-3 nanohybrid electrodes using GCD at a 10 A/g for 10,000 cycles. The MVO, MVOG-1, MVOG-2, and MVOG-3 bare nanohybrid retained 85.28%, 89.32%, 93.16%, and 90.73% of their original capacity, indicating that the nanohybrid electrodes exhibit appropriate capacity retention. The optimized MVOG-2 nanohybrid electrode shows the maximum capacity retention compared to those of bare MVO and other MVOG-1 and MVOG-3 nanohybrid electrodes.

Also, the variation of specific capacity with scan rate is represented in Figure S9(f). At higher current density and scan rates, specific capacity decreases due to insufficient dissemination of ions in the MVO and MVOG electrodes. The specific capacity of all MVOG electrodes is higher than that of the bare MVO electrode. Among all MVOG electrodes, the MVOG-2 has the highest specific capacity providing its ability to charge−discharge quickly. Using the galvanostatic charge−discharge graphs, the MVO electrode shows a maximum

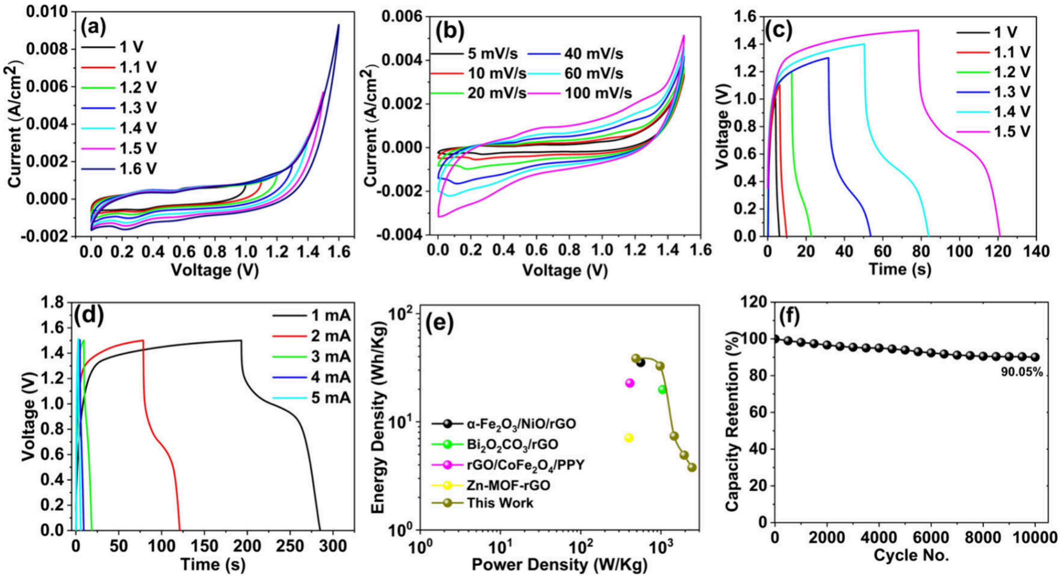

Figure 6. CV plot of HSC at different (a) operating potential windows (1−1.6 V) and (b) sweep rates (5−100 mV/s). GCD plot of HSC at different (c) operating potential windows (1−1.5 V) and (d) currents (1−5 mA). (e) HSC Ragone graph. (f) Capacity retention of HSC at 10 A/g using GCD for 10,000 successive cycles.

capacity of 188.86 C/g at 2 A/g. The optimal MVOG-2 nanohybrid electrode has a capacity of 796.25 C/g at 2 A/g and retains 67% of its initial value of 535.10 C/g at 6 A/g. Furthermore, the increase in GO concentration reduces the value of the specific capacity to 543.13 C/g at 2 A/g. As a result, hybridization significantly improves the rate capability and quick charge transport. Thus, the MVOG-2 nanohybrid material is used to create the HSC device. A comparative table of CV and charge−discharge (CD) calculations of MVO and MVOG-1, -2, and -3 electrodes and HSC device is shown in Table S18.

The electrochemical impedance study of bare MVO and MVOG nanohybrid electrodes was carried out in the higher and lower frequency regions, as depicted in Figure S14. From the studies, the solution resistance (R_s), the charge transfer resistance R_{ct}, and the Warburg resistance W of all MVOG hybrid electrodes and bare MVO are shown in Table S19. The Nyquist graph of MVO and MVOG nanohybrid material does not exhibit a semicircle at the high-frequency range; hence, the charge transfer resistance (R_{ct}) is also much less. It is observed that the values of R_s and R_{ct} for the optimized MVOG-2 electrode are lower than for the MVO, MVOG-1, and MVOG-3 electrodes, resulting in high charge transfer and conductivity of the MVOG electrode. In the lower frequency region, the plot of the MVOG-2 electrode is steeper, resulting in a low W and higher electrical conductivity among the MVOG electrodes. This indicates a fast charge transfer and high conductivity of the MVOG electrodes. Among the MVOG electrodes, the MVOG-2 electrode shows a higher conductivity. Hence MVOG-2 was preferred for fabrication of HSC device.

3.5. Hybrid Supercapacitor (HSC).

The HSC was employed to validate the practicality of the MVOG-2 nanohybrid electrode. The electrochemical performance of HSC was studied using 2-electrode system. In HSC, 2 M KOH was an electrolyte, and rGO and MVOG-2 were used as the anode and cathode, respectively. Highly porous glass was used as a separator. They were all assembled into a portable electrochemical cell (EC-cell). Thus, the prepared EC-cell is designated as MVOG//rGO throughout the manuscript. GO is reduced to rGO in a hydrothermal process and used as an anode in HSC. The composition of rGO in bare MVOG-2 enhances the electrochemical properties of bare MVO because of the inherent properties of rGO.[57] The CV, GCD, and EIS were performed for MVOG//rGO (EC-cell). The schematic representation of the EC-cell is shown in Figure S16. The energy density can be enhanced by increasing either C or V using an $E = 1/2CV^2$ equation. In the three electrode setup, the maximum potential window (V) for MVO and MVOG is 0.6 V. Hence, we fabricate the HSC by adding both electrodes to the extended window, 0.6 + 1.0 = 1.6 V. Figure S17 shows the extension of the potential window of MVOG and rGO for a 20 mV/s scan rate. In the HSC, the optimized potential window of 1.5 V is utilized to enhance the energy and power density.

The CV graph of the rGO electrode is shown in Figure S15(a), which has a potential window (−1.0 to 0 V) at sweep rates of 5, 10, 20, 50, and 100 mV/s. The GCD plot of rGO is shown in Figure S15(b) in the potential window −1.0 to 0 V at 1−8 A/g various current densities. Also, Figure S15(c) shows the EIS of the rGO electrode. Therefore, the HSC's optimized potential window can be 0−1.5 V to obtain the high specific energy (SE) of the HSC. Figure 6(a) depicts the CV plot at varying potential windows (1−1.6 V) at a sweep rate of 100 mV/s, to analyze charge storage and charge mobility across the HSC electrode. Figure 6(b) shows the CV plot of HSC at sweep rates of 5,10, 20, 40, 60, and 100 mV/s at a potential window of 1.5 V.

Also, the GCD plots of HSC at different operating potential windows ranging from 1 to 1.5 V are shown in Figure 6(c). The HSC GCD plots at 1−5 mA are shown in Figure 6(d) in an operating potential window of 1.5 V. Figure 6(e) presents comparative Ragone plots of various reported nanohybrid materials and the present work. To obtain a high SE value, a wider and optimized operating potential window was used for the maximum current response. The HSC exhibits a maximum energy density of 38.55 Wh/kg (at 1 mA) and a power density of 2434.38 W/kg (at 5 mA). The HSC device shows a maximum capacity retention of 90.05% of its original value over 10,000 cycles at 10 A/g, as shown in Figure 6(f). The

SEM analysis of MVO and MVOG-2 electrodes after cyclic stability over 10,000 cycles is investigated and shown in Figure S20.

In addition, a comparison table of the energy and power densities of the reported nanohybrid material is shown in Table S20. Thus, the electrochemical performance of our HSC (MVOG) was reported for the first time and exhibits the superior performance of a supercapacitor. The electrochemical study of the HSC gives the highest specific capacity of 185.06 C/g at 1 mA. The electrochemical impedance of the HSC device shows hybridization of MVO with rGO resulting in higher conductivities. Figure S19(a) represents the variation of specific capacity with current. Figure S19(b) shows the Nyquist plot of the MVOG//rGO (EC-cell) and the values of the equivalent circuits R_s and R_{ct} are 0.6933Ω and 0.682Ω, respectively. These values are very small, resulting in higher conductivities.

4. CONCLUSIONS

In this work, MVO and MVOG nanohybrids were successfully synthesized by the chemical route of the hydrothermal method. The synthesized MVO nanostructures show a flower-like morphology, and the MVOG nanohybrids confirm nanostrips wrapped with rGO nanosheets that increase porosity, conductivity, and overall electrochemical properties. Variations in the GO content in MVO are noticeable in the electrochemical performance of MVOG nanohybrids. The optimal MVOG-2 electrode exhibits a maximum capacity of 714.85 C/g, which is much higher than the bare MVO of 270.73 C/g at a sweep rate of 2 mV/s. HSC fabrication using positive and negative MVOG-2 and rGO electrodes was also used. The HSC delivered the highest capacity of 185.06 C/g at 1 mA and the corresponding maximum energy and power densities of 38.55 Wh/kg and 2434.38 W/kg, respectively. The HSC device exhibits an excellent long cyclic stability of 90.05% over 10,000 successive GCD cycles at 10 A/g. Thus, hybridization with rGO enhances the overall electrochemical performance of bare MVO. Hence, using the hydrothermal method, hybridization of different binary transition metal oxides with rGO can be prepared.

■ ASSOCIATED CONTENT

Supporting Information

The Supporting Information is available free of charge at https://pubs.acs.org/doi/10.1021/acs.energyfuels.4c00094.

> Detailed experimental procedure, XPS of all MVOG nanohybrids (Figures S1−S3), SEM of MVOG-2 (Figure S4), HRTEM and SAED of MVO and MVOG-2 nanohybrids (Figure S5), interplanar spacing (Figure S6), line mapping (Figure S7), EDS line mapping (Figure S8), electrochemical studies (CV, GCD, and stability) of MVOG-1 and MVOG-3 (Figure S9), charge separation study of MVO and MVOG nanohybrids (Figure S10), electrochemical kinetics measurement of MVO (Figure S11), MVOG-1 (Figure S12), and MVOG-3 (Figure S13), electrochemical impedance spectroscopy of MVO and MVOG nanohybrids (Figure S14), electrochemical studies of rGO (Figure S15), HSC device schematics representation (Figure S16), combined potential window (Figure S17), correlation between redox peak with oxidation states (Figure S18), Ragone plot and EIS (Figure S19), SEM of MVO and MVOG-2 after 10,000 GCD cycle (Figure S20), calculations for interplanar spacing MVOG-2 (Table S1), binding energy comparison for all MVO and MVOG nanohybrids (Table S2), peak positions, FWHM, and % relative peak intensity (Tables S3−S5), quantitative analysis (Tables S6−S9), C/O ration (Table S10), elemental composition (Table S11), SAED calculations (Table S12), HRTEM line mapping (Table S13), electrochemical parameters (Tables S14 and S20), diffusion coefficient and *b* value calculation (Table S15), and anodic and cathodic K_1 and K_2 values for MVOG-2 (Tables S16 and S17), comparison of specific capacity for MVO and MVOG nanohybrids (Table S18), ESR values for MVO and MVOG (Table S19) (PDF)

■ AUTHOR INFORMATION

Corresponding Authors

Rajesh K. Nimat − *Department of Physics, Balasaheb Desai College, Patan 415206, India*; Email: rajeshknimat@gmail.com

Jung Bin In − *Soft Energy Systems and Laser Applications Laboratory, School of Mechanical Engineering and Department of Intelligent Energy and Industry, Chung-Ang University, Seoul 06974, Republic of Korea*; orcid.org/0000-0002-9418-9873; Email: jbin@cau.ac.kr

Ji Man Kim − *Department of Chemistry, Sungkyunkwan University, Suwon 16419, Republic of Korea*; orcid.org/0000-0003-0860-4880; Email: jimankim@skku.edu

Ravindra N. Bulakhe − *Department of Chemistry, Sungkyunkwan University, Suwon 16419, Republic of Korea; Soft Energy Systems and Laser Applications Laboratory, School of Mechanical Engineering, Chung-Ang University, Seoul 06974, Republic of Korea*; Email: bulakhe@cau.ac.kr, bulakhe@skku.edu

Authors

Ganesh V. Dilwale − *Department of Physics, R.N.C. Arts, J.D.B. Commerce and N.S.C. Science College, Nashik 422101, India*

Anuradha C. Pawar − *Department of Applied Science and Maths, K.K. Wagh Institute of Engineering Education and Research, Nashik 422003, India*; orcid.org/0000-0002-8550-3971

Guanghai Piao − *Department of Chemistry, Sungkyunkwan University, Suwon 16419, Republic of Korea*; orcid.org/0009-0008-6101-1607

Qian Wang − *Department of Chemistry, Sungkyunkwan University, Suwon 16419, Republic of Korea*

Zafar Said − *Department of Sustainable & Renewable Energy Engineering, University of Sharjah, Sharjah, United Arab Emirates; Department of Industrial and Mechanical Engineering, Lebanese American University (LAU), Byblos 4M8F+6QF, Lebanon*

Complete contact information is available at: https://pubs.acs.org/10.1021/acs.energyfuels.4c00094

Notes

The authors declare no competing financial interest.

■ ACKNOWLEDGMENTS

This research was supported by the Industrial Technology Innovation Program (No. 20007058, Development of safe and comfortable human augmentation hybrid robot suit) funded by the Ministry of Trade, Industry & Energy (MOTIE, Korea) and the National Research Foundation of Korea (NRF) grant funded by the Korea government (MSIT) (No. NRF-2022R1A2C1010296). Also, this work was supported by the National Research Foundation of Korea (NRF) grant funded by the Korea government (MSIT, NRF-2022R1A4A1032832).

■ REFERENCES

(1) Chatterjee, D. P.; Nandi, A. K. A review on the recent advances in hybrid supercapacitors. *J. Mater. Chem. A Mater.* **2021**, *9*, 15880−15918.

(2) Modafferi, V.; Santangelo, S.; Fiore, M.; Fazio, E.; Triolo, C.; Patanè, S.; Ruffo, R.; Musolino, M. G. Transition Metal Oxides on Reduced Graphene Oxide Nanocomposites: Evaluation of Physicochemical Properties. *J. Nanomater* **2019**, *2019*, 1−9.

(3) Raza, W.; Ali, F.; Raza, N.; Luo, Y.; Kim, K.-H.; Yang, J.; Kumar, S.; Mehmood, A.; Kwon, E. E. Recent advancements in supercapacitor technology. *Nano Energy* **2018**, *52*, 441−473.

(4) Ding, Y.; Tang, S.; Han, R.; Zhang, S.; Pan, G.; Meng, X. Iron oxides nanobelt arrays rooted in nanoporous surface of carbon tube textile as stretchable and robust electrodes for flexible supercapacitors with ultrahigh areal energy density and remarkable cycling-stability. *Sci. Rep* **2020**, *10*, 11023.

(5) Jia, B.; Zhang, B.; Cai, Z.; Yang, X.; Li, L.; Guo, L. Construction of amorphous/crystalline heterointerfaces for enhanced electrochemical processes. *EScience* **2023**, *3*, No. 100112.

(6) Benoy, S. M.; Pandey, M.; Bhattacharjya, D.; Saikia, B. K. Recent trends in supercapacitor-battery hybrid energy storage devices based on carbon materials. *J. Energy Storage* **2022**, *52*, No. 104938.

(7) Shaikh, N. S.; Ubale, S. B.; Mane, V. J.; Shaikh, J. S.; Lokhande, V. C.; Praserthdam, S.; Lokhande, C. D.; Kanjanaboos, P. Novel electrodes for supercapacitor: Conducting polymers, metal oxides, chalcogenides, carbides, nitrides, MXenes, and their composites with graphene. *J. Alloys Compd.* **2022**, *893*, No. 161998.

(8) Ren, M.; Di, J.; Chen, W. Recent Progress and Application Challenges of Wearable Supercapacitors. *Batter Supercaps* **2021**, *4*, 1279−1290.

(9) Saravanakumar, B.; Ravi, G.; Ganesh, V.; Guduru, R. K.; Yuvakkumar, R. MnCo2O4 nanosphere synthesis for electrochemical applications. *Mater. Sci. Energy Technol.* **2019**, *2*, 130−138.

(10) Gao, X.; Wang, W.; Bi, J.; Chen, Y.; Hao, X.; Sun, X.; Zhang, J. Morphology-controllable preparation of NiFe2O4 as high performance electrode material for supercapacitor. *Electrochim. Acta* **2019**, *296*, 181−189.

(11) Hao, C.; Zhou, S.; Wang, J.; Wang, X.; Gao, H.; Ge, C. Preparation of Hierarchical Spinel $NiCo_2O_4$ Nanowires for High-Performance Supercapacitors. *Ind. Eng. Chem. Res.* **2018**, *57*, 2517−2525.

(12) Wu, C.; Chen, L.; Lou, X.; Ding, M.; Jia, C. Fabrication of Cobalt-Nickel-Zinc Ternary Oxide Nanosheet and Applications for Supercapacitor Electrode. *Front Chem.* **2018**, *6*, 597.

(13) Sundaram, M. M.; Appadoo, D. Traditional salt-in-water electrolyte *vs.* water-in-salt electrolyte with binary metal oxide for symmetric supercapacitors: capacitive *vs.* faradaic. *Dalton Transactions* **2020**, *49*, 11743−11755.

(14) Jiang, H.; Sun, W.; Li, W.; Wang, Z.; Zhou, X.; Wu, Z.; Bai, J. Facile Synthesis of Novel V0.13Mo0.87O2.935 Nanowires With High-Rate Supercapacitive Performance. *Front Chem.* **2019**, *7*, 595.

(15) Purushothaman, K. K.; Cuba, M.; Muralidharan, G. Supercapacitor behavior of α-MnMoO4 nanorods on different electrolytes. *Mater. Res. Bull.* **2012**, *47*, 3348−3351.

(16) Hong Trang, N. T.; Lingappan, N.; Shakir, I.; Kang, D. J. Growth of single-crystalline β-Na0.33V2O5 nanowires on conducting substrate: A binder-free electrode for energy storage devices. *J. Power Sources* **2014**, *251*, 237−242.

(17) Chatterjee, D. P.; Nandi, A. K. A review on the recent advances in hybrid supercapacitors. *J. Mater. Chem. A Mater.* **2021**, *9*, 15880−15918.

(18) Erdemir, F.; Güler, O.; Çanakçı, A. Electroless nickel-phosphorus coated expanded graphite paper: Binder-free, ultra-thin, and low-cost electrodes for high-performance supercapacitors. *J. Energy Storage* **2021**, *44*, No. 103364.

(19) Muzaffar, A.; Ahamed, M. B.; Deshmukh, K.; Thirumalai, J. A review on recent advances in hybrid supercapacitors: Design, fabrication and applications. *Renewable and Sustainable Energy Reviews* **2019**, *101*, 123−145.

(20) Smith, A. T.; LaChance, A. M.; Zeng, S.; Liu, B.; Sun, L. Synthesis, properties, and applications of graphene oxide/reduced graphene oxide and their nanocomposites. *Nano Materials Science* **2019**, *1*, 31−47.

(21) Patil, S. S.; Dubal, D. P.; Deonikar, V. G.; Tamboli, M. S.; Ambekar, J. D.; Gomez-Romero, P.; Kolekar, S. S.; Kale, B. B.; Patil, D. R. Fern-like rGO/$BiVO_4$ Hybrid Nanostructures for High-Energy Symmetric Supercapacitor. *ACS Appl. Mater. Interfaces* **2016**, *8*, 31602−31610.

(22) Mehrez, J.A.-A.; Owusu, K. A.; Chen, Q.; Li, L.; Hamwi, K.; Luo, W.; Mai, L. Hierarchical $MnCo_2O_4$@$NiMoO_4$ as free-standing core−shell nanowire arrays with synergistic effect for enhanced supercapacitor performance. *Inorg. Chem. Front* **2019**, *6*, 857−865.

(23) Mummoorthi, G.; Shajahan, S.; Abu Haija, M.; Mahalingam, U.; Rajendran, R. Synthesis and Characterization of Ternary α-Fe_2O_3/NiO/rGO Composite for High-Performance Supercapacitors. *ACS Omega* **2022**, *7*, 27390−27399.

(24) Ishaq, S.; Moussa, M.; Kanwal, F.; Ehsan, M.; Saleem, M.; Van, T. N.; Losic, D. Facile synthesis of ternary graphene nanocomposites with doped metal oxide and conductive polymers as electrode materials for high performance supercapacitors. *Sci. Rep* **2019**, *9*, 5974.

(25) Geerthana, M.; Prabhu, S.; Ramesh, R. Hierarchical α-Fe2O3/MnO2/rGO ternary composites as an electrode material for high performance supercapacitors application. *J. Energy Storage* **2022**, *47*, No. 103529.

(26) Yan, B.; Li, X.; Fu, X.; Zhang, L.; Bai, Z.; Yang, X. An elaborate insight of lithiation behavior of V2O5 anode. *Nano Energy* **2020**, *78*, No. 105233.

(27) Wu, D.; Shen, R.; Yang, R.; Ji, W.; Jiang, M.; Ding, W.; Peng, L. Mixed Molybdenum Oxides with Superior Performances as an Advanced Anode Material for Lithium-Ion Batteries. *Sci. Rep* **2017**, *7*, 44697.

(28) Yu, H.; Zeng, J.; Hao, W.; Zhou, P.; Wen, X. Mo-doped V2O5 hierarchical nanorod/nanoparticle core/shell porous microspheres with improved performance for cathode of lithium-ion battery. *J. Nanopart. Res.* **2018**, *20*, 135.

(29) Guru Prakash, N.; Dhananjaya, M.; Purusottam Reddy, B.; Sivajee Ganesh, K.; Lakshmi Narayana, A.; Hussain, O. M. Molybdenum doped V2O5 Thin Films electrodes for Supercapacitors. *Mater. Today Proc.* **2016**, *3*, 4076−4081.

(30) Jovanović, A.; Dobrota, A. S.; Rafailović, L. D.; Mentus, S. V.; Pašti, I. A.; Johansson, B.; Skorodumova, N. V. Structural and electronic properties of V_2O_5 and their tuning by doping with 3d elements − modelling using the DFT+ *U* method and dispersion correction. *Phys. Chem. Chem. Phys.* **2018**, *20*, 13934−13943.

(31) Bulakhe, R. N.; Lee, J.; Tran, C. V.; In, J. B. Mesoporous nanohybrids of 2D layered Cu−Cr phosphate and rGO for high-performance asymmetric hybrid supercapacitors. *J. Alloys Compd.* **2022**, *926*, No. 166864.

(32) Suresh, R.; Giribabu, K.; Manigandan, R.; Kumar, S. P.; Munusamy, S.; Muthamizh, S.; Stephen, A.; Narayanan, V. New electrochemical sensor based on Ni-doped V2O5 nanoplates modified glassy carbon electrode for selective determination of dopamine at nanomolar level. *Sens Actuators B Chem.* **2014**, *202*, 440−447.

(33) Modafferi, V.; Trocino, S.; Donato, A.; Panzera, G.; Neri, G. Electrospun V2O5 composite fibers: Synthesis, characterization and ammonia sensing properties. *Thin Solid Films* **2013**, *548*, 689−694.

(34) Khandare, L.; Late, D. J. MoO3-rGO nanocomposites for electrochemical energy storage. *Appl. Surf. Sci.* **2017**, *418*, 2−8.

(35) Sediri, F.; Gharbi, N. From crystalline V2O5 to nanostructured vanadium oxides using aromatic amines as templates. *J. Phys. Chem. Solids* **2007**, *68*, 1821−1829.

(36) Castillo, C.; Buono-Core, G.; Manzur, C.; Yutronic, N.; Sierpe, R.; Cabello, G.; Chornik, B. Molybdenum Trioxide Thin Films Doped with Gold Nanoparticles Grown by a Sequential Methodology: Photochemical Metal-Organic Deposition (Pmod) And Dc-Magnetron SputterinG. *Journal of the Chilean Chemical Society* **2016**, *61*, 2816−2820.

(37) Khademi, A.; Azimirad, R.; Zavarian, A. A.; Moshfegh, A. Z. Growth and Field Emission Study of Molybdenum Oxide Nanostars. *J. Phys. Chem. C* **2009**, *113*, 19298−19304.

(38) Silversmit, G.; Depla, D.; Poelman, H.; Marin, G. B.; De Gryse, R. Determination of the V2p XPS binding energies for different vanadium oxidation states (V5+ to V0+). *J. Electron Spectrosc. Relat. Phenom.* **2004**, *135*, 167−175.

(39) Silversmit, G.; Depla, D.; Poelman, H.; Marin, G. B.; De Gryse, R. Determination of the V2p XPS binding energies for different vanadium oxidation states (V5+ to V0+). *J. Electron Spectrosc. Relat. Phenom.* **2004**, *135*, 167−175.

(40) Martin, R.; Kim, M.; Lee, C. J.; Mehar, V.; Albertin, S.; Hejral, U.; Merte, L. R.; Lundgren, E.; Asthagiri, A.; Weaver, J. F. High-Resolution X-ray Photoelectron Spectroscopy of an IrO_2 (110) Film on Ir(100). *J. Phys. Chem. Lett.* **2020**, *11*, 7184−7189.

(41) Greczynski, G.; Hultman, L. The same chemical state of carbon gives rise to two peaks in X-ray photoelectron spectroscopy. *Sci. Rep* **2021**, *11*, 11195.

(42) Nguyen, H. T. T.; Jung, D.; Park, C.-Y.; Kang, D. J. Synthesis of single-crystalline sodium vanadate nanowires based on chemical solution deposition method. *Mater. Chem. Phys.* **2015**, *165*, 19−24.

(43) Lee, Y.; Lee, J.; Chung, H.; Kim, J.; Lee, Z. In Situ Scanning Transmission Electron Microscopy Study of MoS_2 Formation on Graphene with a Deep-Learning Framework. *ACS Omega* **2021**, *6*, 21623−21630.

(44) Shireesha, K.; Chidurala, S. C. Impact of hybridization on specific capacitance in hybrid NiO/V2O5@graphene composites as advanced supercapacitor electrode materials. *Applied Surface Science Advances* **2022**, *12*, No. 100329.

(45) Kumbhar, S.S.; Bhosale, S.B.; Pujari, S.S.; Patil, V. V.; Kumar, N.; Salunkhe, R.R.; Lokhande, C.D.; Patil, U.M. Growth Dynamics-Dependent Chemical Approach to Accomplish Nanostructured Cobalt Vanadium Oxide Thin Film Electrodes with Controlled Surface Area for High-Performance Solid-State Hybrid Supercapacitor Devices. *Energy Technology* **2023**, *11*, 2300400.

(46) Portales, M. V.; Lazo Fraga, A. R.; Díaz García, A. M.; García-Zaldívar, O.; Peláiz Barranco, A.; Aguilar Frutis, M. A. Cyclic voltammetry and impedance spectroscopy analysis for graphene-modified solid-state electrode transducers. *J. Solid State Electrochem.* **2018**, *22*, 471−478.

(47) Jacob, G. M.; Zhitomirsky, I. Diffusion-Controlled Electrosynthesis of Nanoporous Electrodes for Electrochemical Supercapacitors. *Journal of Nano Research* **2009**, *7*, 87−92.

(48) Bulakhe, R. N.; Lee, J.; Tran, C. V.; In, J. B. Mesoporous nanohybrids of 2D layered Cu−Cr phosphate and rGO for high-performance asymmetric hybrid supercapacitors. *J. Alloys Compd.* **2022**, *926*, No. 166864.

(49) Li, X.; Zheng, Q.; Li, C.; Liu, G.; Yang, Q.; Wang, Y.; Sun, P.; Tian, H.; Wang, C.; Chen, X.; Shao, J. Bubble Up Induced Graphene Microspheres for Engineering Capacitive Energy Storage. *Adv. Energy Mater.* **2023**, *13*, 2203761.

(50) Kumar, R.; Singh, R. K.; Vaz, A. R.; Savu, R.; Moshkalev, S. A. Self-Assembled and One-Step Synthesis of Interconnected 3D Network of Fe_3O_4 /Reduced Graphene Oxide Nanosheets Hybrid for High-Performance Supercapacitor Electrode. *ACS Appl. Mater. Interfaces* **2017**, *9*, 8880−8890.

(51) Jo, Y. K.; Tamakloe, W.; Jin, X.; Lim, J.; Patil, S. B.; Kang, Y.-M.; Hwang, S.-J. Multilayer hybrid nanosheet of mesoporous carbon−layered metal oxide as a highly efficient electrocatalyst for Li−O2 batteries. *Appl. Catal., B* **2019**, *254*, 523−530.

(52) Ke, Q.; Wang, J. Graphene-based materials for supercapacitor electrodes – A review. *Journal of Materiomics* **2016**, *2*, 37−54.

(53) Yu, H.; Zeng, J.; Hao, W.; Zhou, P.; Wen, X. Mo-doped V2O5 hierarchical nanorod/nanoparticle core/shell porous microspheres with improved performance for cathode of lithium-ion battery. *J. Nanopart. Res.* **2018**, *20*, 135.

(54) Kaveevivitchai, W.; Jacobson, A. J. High Capacity Microporous Molybdenum−Vanadium Oxide Electrodes for Rechargeable Lithium Batteries. *Chem. Mater.* **2013**, *25*, 2708−2715.

(55) Choi, H.; Nguyen, P. T.; Tran, C. V.; In, J. B. Micro-patterned metal current collectors for high aspect ratio flexible graphene supercapacitors. *Appl. Surf. Sci.* **2020**, *510*, No. 145432.

(56) El-Kady, M. F.; Ihns, M.; Li, M.; Hwang, J. Y.; Mousavi, M. F.; Chaney, L.; Lech, A. T.; Kaner, R. B. Engineering three-dimensional hybrid supercapacitors and microsupercapacitors for high-performance integrated energy storage. *Proc. Natl. Acad. Sci. U. S. A.* **2015**, *112*, 4233−4238.

(57) Smith, A. T.; LaChance, A. M.; Zeng, S.; Liu, B.; Sun, L. Synthesis, properties, and applications of graphene oxide/reduced graphene oxide and their nanocomposites. *Nano Materials Science* **2019**, *1*, 31−47.